Upper crustal seismic structure of the Endeavour Segment, Juan de Fuca Ridge from travel time tomography: Implications for oceanic crustal accretion

Supplementary Documents

Robert T. Weekly[1], William S.D. Wilcock[2], Douglas R. Toomey[3], Emilie E.E. Hooft[3], Eunyoung Kim[4]

(1) Department of Earth and Space Sciences, University of Washington, Box 351310, Seattle, WA 98195-1310
(2) School of Oceanography, University of Washington, Box 357940, Seattle, WA 98195-7940
(3) Department of Geological Sciences, University of Oregon, 1272 University of Oregon, Eugene, OR 97403-1272
(4) School of Earth and Environmental Sciences, Seoul National University, Seoul, Korea, Republic of

Supplementary Documents

S1. Derivative Weight Sum

To delimit the volume in which our preferred model is well resolved, we analyzed the spatial distribution of ray paths. A spatial measure of the distribution of *Pg* ray paths within the experiment footprint is given by the derivative weight sum (DWS) [*Thurber*, 1983; *Toomey and Foulger*, 1989], which calculates the weighted sum of path lengths influencing each node in the perturbational grid. In short, DWS is a unitless number that describes the influence of ray path density on perturbational grid nodes, and interpretations drawn from results lying below a DWS threshold should be avoided. From inspection of the checkerboard tests (see below), we set a DWS threshold of 10 for masking our models. Selecting a precise value was somewhat subjective and depended on the wavelength of the feature of interest, but DWS increased rapidly inside the minimum contour in most of the model space (Figure S1). Ray path distribution in the upper crust was sparse at the outer edges of the experiment and dense within the centralized crustal grid to depths of ~3 km. There was a paucity of ray paths sampling crustal structure below 3 km depth near the central Endeavour segment. This data-limited region of our model resulted from the presence of the AMC located 2 – 3 km beneath the central axial valley [*Van Ark et al.*, 2007], which limited the ranges at which *Pg* could be easily identified.

S2. Synthetic Isotropic Inversions

To assess the resolution of our results, we used reconstructions of several types of synthetic models. For all synthetic models, we calculated predicted *Pg* travel-times for the same station-receiver pairs as in our experiment, assigned 10 ms of uncertainty to each arrival time, and inverted the data using the same parameters as in our preferred solutions.

We tested the resolution of isotropic structure by constructing synthetic models of checkerboard pattern velocity anomalies that consisted of 5% velocity perturbations applied to the average one-dimensional velocity structure (solid black line in Figure 4a) and alternated between positive and negative anomalies. All the checkerboard tests show that the tomographic inversion has a tendency to underestimate the magnitude of velocity anomalies even in the best resolved regions.

To evaluate the resolution of segment-scale features, we used columnar checkerboard tiles measuring 10, 15, and 20 km on a side in which the polarity of the perturbations did not alternate with model depth. Figure S2 shows map-view sections of the reconstructed anomalies for the 10-km–by-10-km tiles. The tests demonstrate that structural features on the order of ~10 km in size are generally well resolved between 0.5 and 2.5 km depth. The checkerboard pattern is best recovered between 1 – 2 km depth (Figure S2b), where the tiles are more clearly outlined and the percentage recovery is highest. At these depths, we are able to resolve anomalies near the E-WV and Cobb OSCs with greater resolution and a higher percentage recovery than at depths shallower than 1 km or deeper than 2 km (Figure S2a and S2c, respectively). A broad distribution of ray paths near the intersection of the overlapping limbs enables good recovery of the velocity perturbations, but a lack of ray paths at the distal ends of the OSCs prevents satisfactory recovery of structure in these regions. Similarly, anomalies between 1 km and 2 km depth are better recovered at off-axis distance exceeding ~20 km compared to crustal structure at other depths. We attribute this to the high density and broad azimuthal distribution of *Pg* ray paths that turn between 1 km and 2 km depth (Figure S1b).

To evaluate the resolution of features located near the more densely-sampled central portion of the segment (Figure S1), we analyzed synthetic checkerboard models with 5-km-by-5-km-by-1-km tiles (Figure S3). Unlike the models of Figure S2, the polarity of the velocity perturbations alternated with depth so we could assess the vertical resolution. Checkerboard anomalies in the upper 1 km are well recovered within 10 km of the ridge but are poorly recovered at larger ranges where they exhibit some horizontal smearing due to poor ray path coverage in the upper crust (Figure S3a). At 1-2 km depth, anomalies are reasonably well recovered near the ridge axis with no evidence for horizontal smearing observed at shallower depths (Figure S3b). Anomalies out to 20 km off-axis are best recovered at these depths (Figure S3). The recovered amplitude of synthetic anomalies at depths greater than ~2 km (Figure S3c) is poor compared to shallower depths, which reflects the small percentage of ray paths turning deeper than ~2 km.

To test the limits of resolution near the hydrothermal fields, we performed inversions of synthetic data from a checkerboard model with 2-km-by-2-km-by-1-km tiles (Figure S4). Recovery of synthetic anomalies indicates that structure near the axial valley is well resolved within the upper 2 km, but the amplitude of the recovered anomalies is higher within the upper 1

km. This synthetic model shows that the resolution of our model is sufficient to resolve features on the scale of the spacing of hydrothermal vents.

S3. Synthetic Anisotropic Inversions

We conducted a series of synthetic models to evaluate the anisotropic component of our inversions. First, to investigate the tradeoff between isotropic and anisotropic structure in the inversion, we considered a synthetic model in which the isotropic component was the average vertical velocity structure of the preferred model (solid line, Figure 4a) and the amplitude of ridge-parallel anisotropy decreased from 5% at the seafloor to 0% at 4 km depth (dashed line in Figure S5). Figures S5 and S6-c show the difference between the starting model and the synthetic model.

The horizontally-averaged recovered anisotropic signal in this inversion is smaller than in the starting model at all depths (Figure S5) and the magnitude of the anisotropic signal tends to decrease off-axis (Figure S6a-c). In order to assess whether this effect might produce the large decrease in the magnitude of anisotropy observed in our preferred model within 5 to 10 km of the ridge axis (Figure 10-11), we conducted a second synthetic anisotropic inversion that was identical to the first except that the magnitude of anisotropy was doubled within 5 km of the ridge axis. Figure S6d-f shows the recovered magnitude of anisotropy at three depths.

Figure S7 shows the change in the average percentage of anisotropy off-axis at different depths for the preferred model and for the two synthetic inversions. It is clear that the synthetic inversion with higher anisotropy near the ridge axis more closely reproduces the change in the magnitude of anisotropy seen off-axis than the model with constant anisotropy. Indeed, it appears that a doubling of anisotropy near the ride axis is insufficient to reproduce the preferred inversion. Thus, we infer that while the inversions will tend to underestimate the magnitude of anisotropy, particularly well off-axis, the large decrease in the magnitude of anisotropy off-axis in the preferred model is a real effect. The preferred inversions also shows significantly larger along-axis variations in the magnitude of anisotropy than the synthetic inversion of Figure S6d-f, so we infer that along-axis variations in the magnitude of anisotropy are required by the data.

To evaluate the ability of the inversions to resolve variations in the magnitude of anisotropy, we used synthetic models with a checkerboard patterns of anisotropy in which the fast direction is everywhere parallel to the ridge axis but the magnitude of anisotropy varies.

Figure S8 shows the recovery for a model with 5-km-by-5-km columnar tiles and a magnitude that in half of the tiles decreased from 5% at the seafloor to 0% at 4 km depth (dashed line in Figure S5) and is twice this in the other half. The results show that the variations in the relative magnitude of anisotropy is well recovered within 10 km of the ridge axis but that the amplitude is everywhere somewhat underestimated. At distances greater than 10 km off axis (i.e., outside the region of the intermediate grid), anisotropy magnitude variations on this length scale are not well resolved.

To evaluate the ability of the inversions to resolve variations in the orientation of the fast direction of anisotropy, we used synthetic models with checkerboard patterns of anisotropy in which the magnitude was constant throughout the model but the fast direction varied. Figure S9 shows the recovery for two models with 10-km-by-10-km columnar tiles and a fast direction that is rotated by 90˚ and 45˚, respectively, between adjacent tiles. Recovery of the synthetic data shows that variations in the orientation of anisotropy near the central portion of the experiment are well resolved, however, the synthetic models are not as well recovered near the margins of the experiment. In these regions, the recovered azimuths are often intermediate between the values of adjacent tiles. We attribute this lack of fine-scale resolution to the relatively poor azimuthal distribution of ray paths near the edges of the experiment.

Supplementary References

Thurber, C. H. (1983), Earthquake locations and three-dimensional crustal structure in the Coyote Lake Area, Central California, *J. Geophys. Res.*, *88*, 8226-8236, doi:10.1029/JB088iB10p08226.

Toomey, D. R., and G. R. Foulger (1989), Tomographic inversion of local earthquake data from the Hengill-Grensdalur Central Volcano Complex, Iceland, *J. Geophys. Res.*, *94*, 17497-17510, doi:10.1029/JB094iB12p17497.

Van Ark, E. M., R. S. Detrick, J. P. Canales, S. M. Carbotte, A. J. Harding, G. M. Kent, M. R. Nedimovic, W. S. D. Wilcock, J. B. Diebold, and J. M. Babcock (2007), Seismic structure of the Endeavour Segment, Juan de Fuca Ridge: Correlations with seismicity and hydrothermal activity, *J. Geophys. Res.*, *112*(B2), B02401, doi:10.1029/2005jb004210.

Supplementary Document Figure Captions

S1) Map-view sections of the derivative weight sum (DWS) at (a) 0.5 km, (b) 2.0 km, and (c) 3.5 km depth contoured at 10, 100 and 1000 to show the relative density of rays.

S2) Map-view slices at (a) 0.4 km, (b) 1.4 km, and (c) 2.4 km depths showing results from synthetic isotropic velocity checkerboard tests for columnar 10-km-by-10-km tiles. Velocity perturbations were ±5% from the preferred isotropic model and perturbations did not vary with depth. Green stars show the locations of vent fields. Solid black lines show the traces of the West Valley, Endeavour, and Northern Symmetric segments. The color contours show the percent recovery of the *P*-wave perturbation with a contour interval of 20%.

S3) Map-view slices at (a) 0.4 km, (b) 1.4 km, and (c) 2.4 km depths showing results from synthetic isotropic velocity checkerboard tests for 5-km-by-5-km-by-2-km tiles. The same plotting conventions are used as for Figure S2.

S4) Map-view slices taken at (a) 0.4 km and (b) 1.4 km depths and (c) vertical cross-section through the vent fields (X = 0 km) showing results from synthetic isotropic velocity checkerboard tests for 2-km-by-2-km-by-1-km tiles. The same plotting conventions are used as for Figure S2.

S5) One-dimensional percent anisotropy structure for a synthetic model used to calculate travel times (dashed line) and the vertical average of the model recovered from the inversion in a region extending 10 km to either side of the ridge axis and from Y = -20 km to Y = 20 km (solid line).

S6) Map-view slices at 0.4 km, 1.2 km and 2 km depth showing the magnitude of anisotropy contoured at 1% intervals for two synthetic inversions. (a–c) Results for the inversion shown in Figure S5 in which the anisotropy in the model used to calculate synthetic travel times varies from 5% at the seafloor to 0% at 4 km depth. (d-f) Results for an

inversion in which the model used to calculate synthetic travel times is the same as before except the magnitude of anisotropy is doubled within 5 km of the ridge axis (-5 km < X < 5 km). The vent fields (green stars) and traces of the segments (bold cyan lines) are also shown.

S7) Plots showing the change in average magnitude of anisotropy as a function of off-axis range for the preferred anisotropic model discussed in the text (black), the synthetic inversion of Figure S6a-c with horizontally invariant anisotropy (red) and the synthetic inversion of Figure S6d-f with the magnitude of anisotropy doubled within 5 km of the ridge axis (blue). Note that the shape of the curves for the second synthetic inversion more closely resembles that for the preferred isotropic model, indicating that the off-axis decrease in anisotropy is well-resolved.

S8) Map view slices of the magnitude of anisotropy contoured at 1% intervals at 0.4 km, 1.0 km and 1.6 km depth for the recovery of a synthetic anisotropic checkerboard model in which the fast direction was oriented along the ridge axis (Y axis). The magnitude of anisotropy varied in alternate 5-km-by-5-km checkers from 10% and 5%, respectively at the seafloor to 0% at 4 km depth following the profile shown by a dashed line in Figure S5. Note that structure is well resolved within 10 km of the axis but that the amplitude of the anisotropy is underestimated.

S9) Map-view slices of the orientation of anisotropy taken at 0.4 km depth for the recovery of synthetic anisotropic checkerboard models for 10-km-by-10-km columnar tiles in which the orientation of seismic anisotropy is perturbed by (a) 90˚ and (b) 45˚. Solid black lines show the orientation and relative magnitude of the fast direction of anisotropy on a 4-km-by-4-km grid. A tick of length 4 km would represent 100% recovery of the anisotropy magnitude. The vent fields (green stars) and traces of the segments (bold black lines) are also shown.

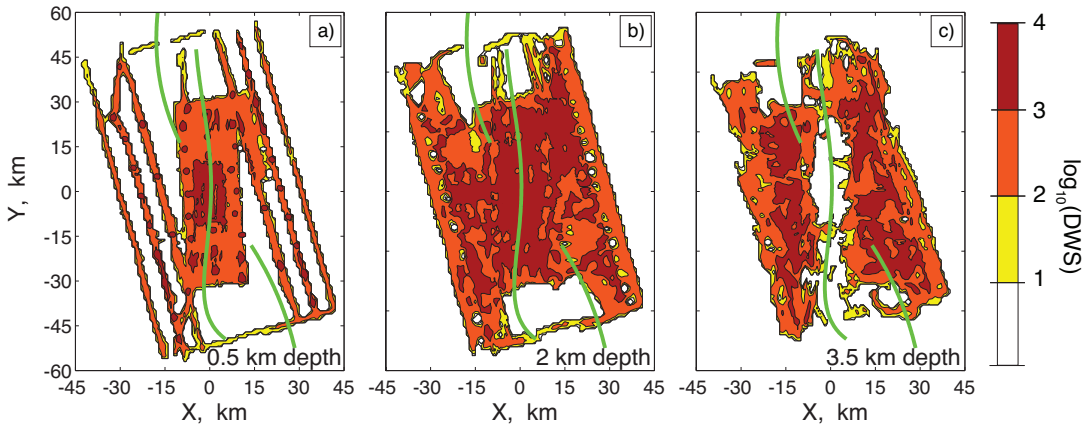
a)
b)
c)
0.5 km depth
2 km depth
3.5 km depth
Y, km
X, km
X, km
X, km
60
45
30
15
0
-15
-30
-45
-60
-45 -30 -15 0 15 30 45
4
3
2
1
log10(DWS)

Figure S1

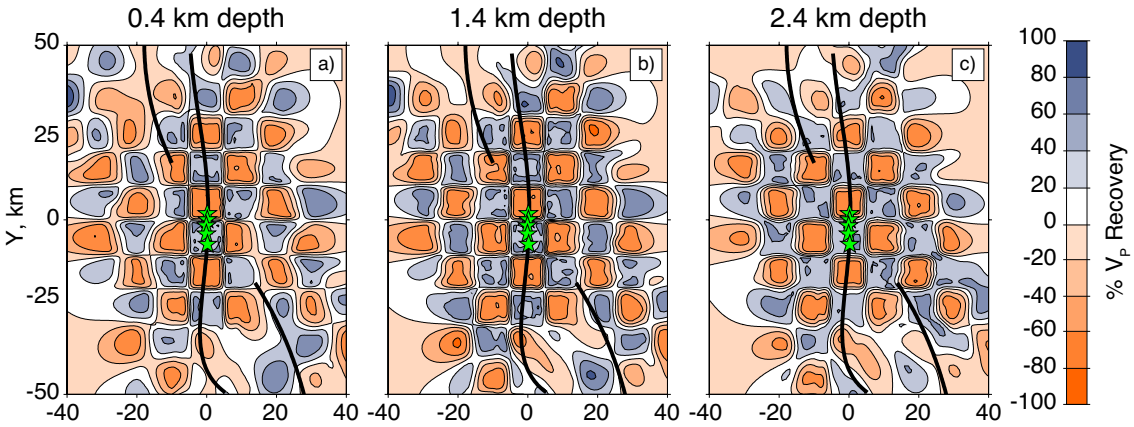
0.4 km depth
1.4 km depth
2.4 km depth
a)
b)
c)
Y, km
50
25
0
-25
-50
-40
-20
0
20
40
100
80
60
40
20
0
-20
-40
-60
-80
-100
% V_P Recovery

Figure S2

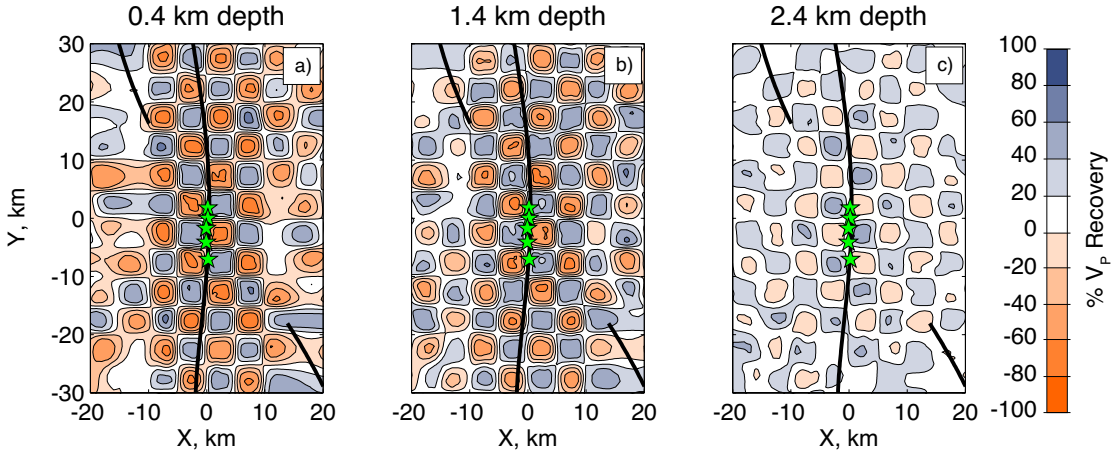
0.4 km depth
1.4 km depth
2.4 km depth
a)
b)
c)
Y, km
X, km
X, km
X, km
30
20
10
0
-10
-20
-30
-20 -10 0 10 20
100
80
60
40
20
0
-20
-40
-60
-80
-100
% V_p Recovery

Figure S3

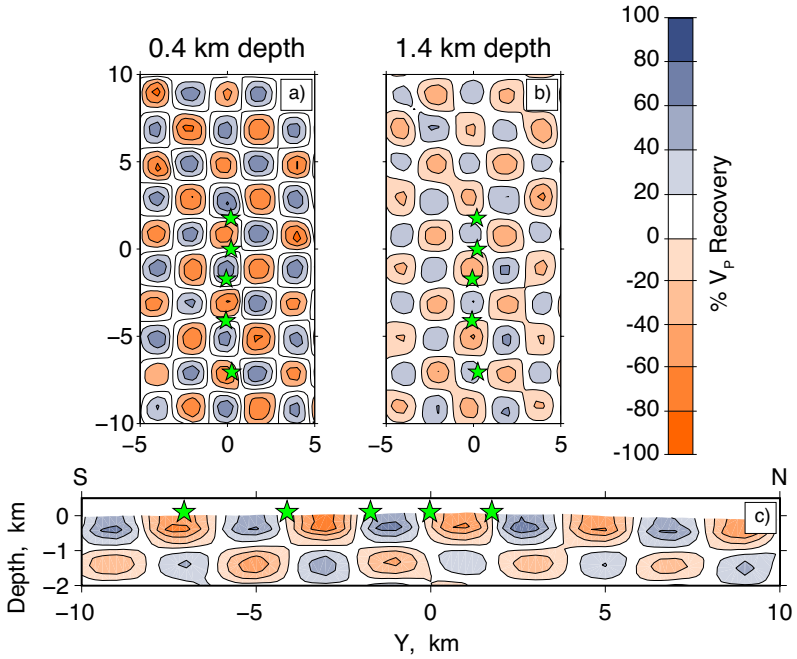
0.4 km depth
1.4 km depth
a)
b)
c)
100
80
60
40
20
0
-20
-40
-60
-80
-100
% V_P Recovery
10
5
0
−5
−10
−5
0
5
S
N
Depth, km
0
−1
−2
−10
−5
0
5
10
Y, km

Figure S4

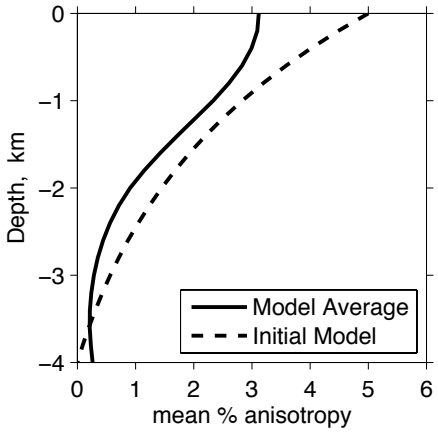
0
−1
−2
−3
−4
Depth, km
0
1
2
3
4
5
6
mean % anisotropy
Model Average
Initial Model

Figure S5

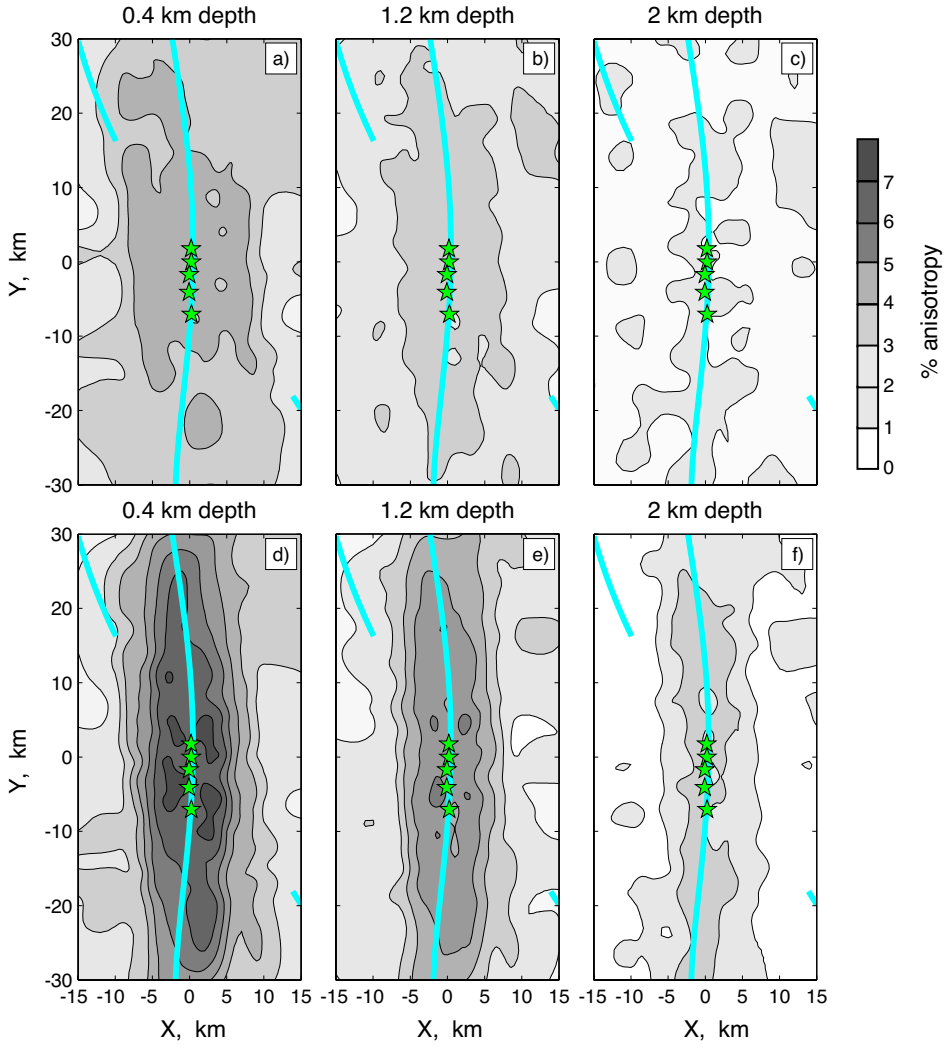
0.4 km depth
1.2 km depth
2 km depth
a)
b)
c)
d)
e)
f)
Y, km
X, km
% anisotropy
30
20
10
0
-10
-20
-30
-15 -10 -5 0 5 10 15
7
6
5
4
3
2
1
0

Figure S6

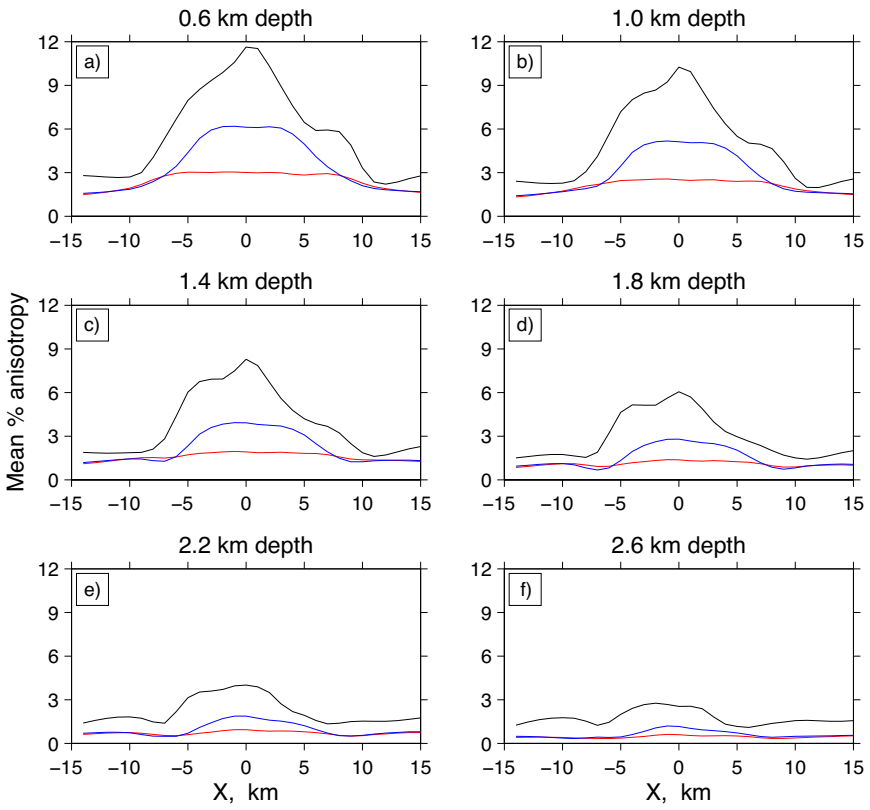
0.6 km depth
1.0 km depth
1.4 km depth
1.8 km depth
2.2 km depth
2.6 km depth
a)
b)
c)
d)
e)
f)
Mean % anisotropy
X, km
X, km
0
3
6
9
12
−15
−10
−5
0
5
10
15

Figure S7

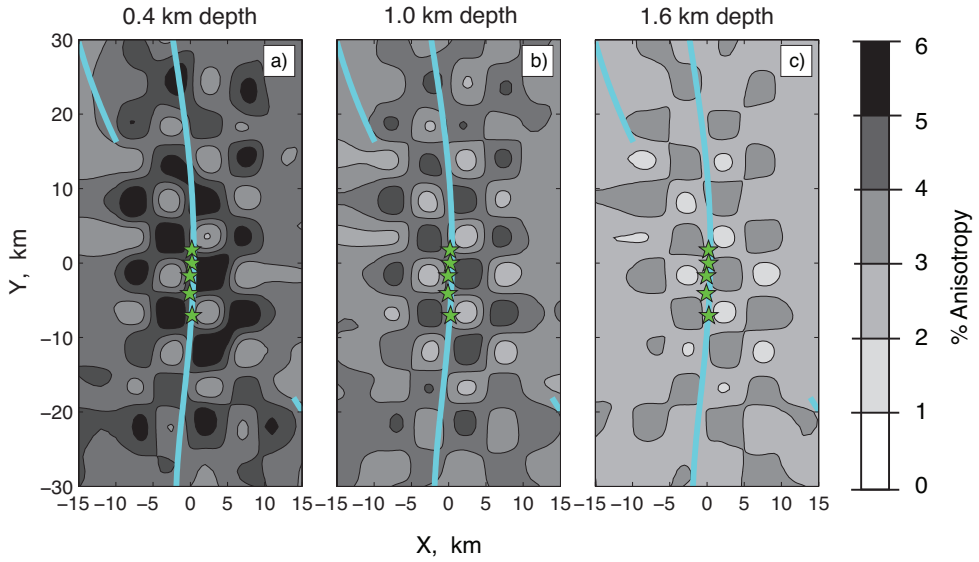
0.4 km depth
1.0 km depth
1.6 km depth
a)
b)
c)
Y, km
X, km
% Anisotropy
30
20
10
0
−10
−20
−30
−15 −10 −5 0 5 10 15
6
5
4
3
2
1
0

Figure S8

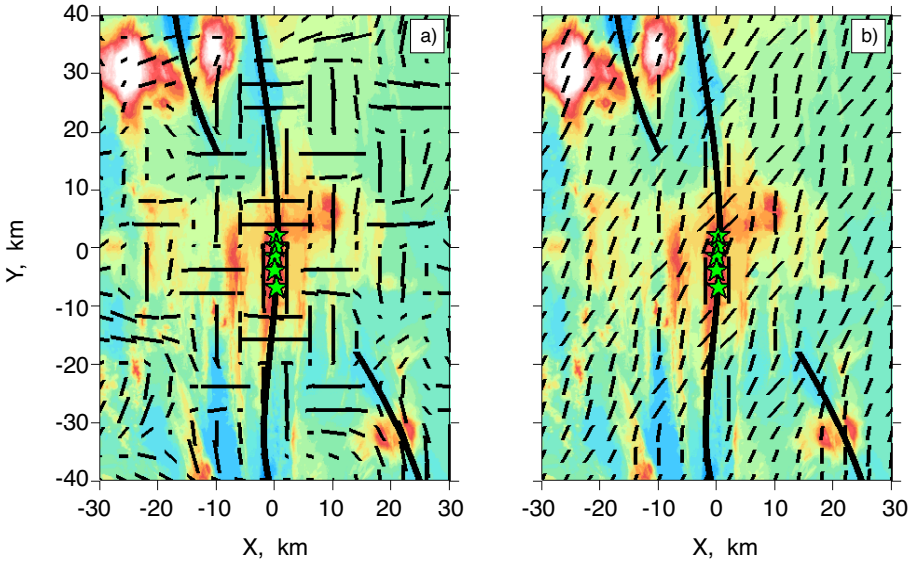

Figure S9